crystals

MDPI

Article

Construction of Oxygen Vacancies of Zr-Doped CeO_2 with Enhanced Dye Adsorption Performance

NingTao Luo [1], Lei Fan [2], YunQiang Chen [2] and WeiGuang Lan [1,*]

[1] Xiamen University Center for Membrane Application and Advancement, College of Materials, Xiamen University, Xiamen 361005, China; luoningtao@stu.xmu.edu.cn
[2] Suntar Membrane Technology (Xiamen) Co., Ltd., Xiamen 361022, China; fanlei@xmu.edu.cn (L.F.); chenyq@suntar.com (Y.C.)
* Correspondence: wglan@xmu.edu.cn

Abstract: Congo red (CR), a highly pigmented anionic dye, is highly toxic and resistant to degradation. The discharge of CR wastewater into the natural environment can lead to ecological destruction and harm to human health. CeO_2 as an adsorbent possesses the advantages of excellent acid and alkali resistance, biocompatibility, stable physical and chemical properties, and nontoxic by-products. The impact of Zr doping on the adsorption performance of nano-CeO_2 was investigated. XPS and Raman characterisation revealed that Zr doping effectively enhanced the oxygen vacancy ratio at the active sites for CR adsorption on the surface of nano-CeO_2. When the doping amount of Zr was 3%, the nanoparticles with the best adsorption properties were obtained, and the adsorption amount of CR at room temperature was as high as 3642.05 mg/g, which was approximately three times the adsorption amount of undoped CeO_2. This excellent adsorption property shows good prospects for the removal of anionic dyes from wastewater.

Keywords: adsorption; oxygen vacancy; Cerium oxide; nano-particles; doping

check for updates

Citation: Luo, N.; Fan, L.; Chen, Y.; Lan, W. Construction of Oxygen Vacancies of Zr-Doped CeO_2 with Enhanced Dye Adsorption Performance. *Crystals* **2023**, *13*, 1641. https://doi.org/10.3390/cryst13121641

Academic Editor: Evgeniy N. Mokhov

Received: 1 November 2023
Revised: 22 November 2023
Accepted: 22 November 2023
Published: 27 November 2023

Copyright: © 2023 by the authors. Licensee MDPI, Basel, Switzerland. This article is an open access article distributed under the terms and conditions of the Creative Commons Attribution (CC BY) license (https://creativecommons.org/licenses/by/4.0/).

1. Introduction

The dyeing, textile, leather, plastic, and other industries generate significant amounts of dye-containing wastewater [1–4]. Anionic dyes such as Congo Red (CR) exhibit intense colouration and chromaticity, lead to a substantial pollution load, and have limited degradation under natural conditions [5,6]. Discharging untreated CR wastewater into the natural environment poses a threat to ecological integrity and carcinogenic and mutagenic risks to living organisms [7,8]. Therefore, the removal of these substances is crucial to safeguard the environment and public health against their deleterious effects. A number of methods have been used to remove CR dye from wastewater, including photocatalytic (redox) reactions, flocculation, coagulation, ion exchange, reverse osmosis, membrane filtration, and adsorption [9–14]. Compared to other techniques, the adsorption technique is best suited for practical applications, since it offers advantages such as operational simplicity, cost-effectiveness, and the generation of non-toxic byproducts, making it widely employed in dye wastewater treatment [15–17]. Metal oxides serve as advanced adsorbents because of their unique characteristics, including their large surface areas, diverse forms, stable chemical properties, and abundant surface functional groups [18–21]. Among the various metal oxides, cerium oxide has garnered special attention for wastewater treatment owing to its nontoxic nature, economic viability, and environmental friendliness [15–17]. Compared to traditional adsorbents, such as activated carbon [22], hydrogels [23], zinc oxide [24], and alumina [25], nano-CeO_2 exhibits superior acid-alkali resistance, biocompatibility, and stable physical/chemical properties [26].

It has been reported that oxygen vacancies play a crucial role as active sites for the adsorption of CR dyes [27,28]. Zhao [27] discovered that increasing the concentration of oxygen vacancies on the surface of Al_2O_3 enhances the adsorption of CR. Joshy [29] used the

sol-gel technique to fabricate Er^{3+}-doped CeO_2 nanoparticles featuring an enhanced surface vacancy density, thus demonstrating the exceptional efficacy and selectivity of Er^{3+}-doped CeO_2 as a potent adsorbent for CR. The oxygen vacancy serves as the primary active site on the surface of CeO_2, and both Ce^{4+} (0.97 Å) and Zr^{4+} (0.86 Å) exhibit similar radii [30]. Upon the introduction of Zr^{4+} into CeO_2, the crystal structure undergoes a distortion, resulting in an increased number of oxygen vacancies generated by Zr^{4+} doping within the CeO_2 lattice, which plays a crucial role in selective adsorption. The oxygen vacancies have a strong affinity for water adsorption, and the adsorbed water molecules can selectively form hydrogen bonds with the NH_2 groups present on CR molecules, thereby enhancing the adsorption rate and equilibrium capacity of CeO_2 nanoparticles towards CR molecules. However, the adsorption properties of Zr-doped CeO_2 systems have not been studied. In this study, we investigated the adsorption behaviour of a Zr-doped CeO_2 system using CR as a representative adsorbent. The experimental results demonstrate that Zr-doped CeO_2 nanoparticles possess a remarkably high adsorption capacity. Furthermore, our findings revealed that the proposed Zr-doped CeO_2 system outperformed the commonly used CeO_2 in terms of its dye adsorption capacity, shown using XPS [31], Raman spectroscopy [32], DFT [33], and neutron diffraction [34] as suitable methods to study oxygen defects. In this study, we have used XPS and Raman spectroscopy to study oxygen defects.

2. Materials and Methods

2.1. Materials

All reagents were used as received without further purification. Cerium nitrate hexahydrate ($Ce(NO_3)_3 \bullet 6H_2O$, 99.99%), Sodium dodecyl benzene sulfonate ($C_{18}H_{29}NaO_3S$, 97%), and Zirconium oxychloride octahydrate ($ZrOCl_2 \bullet 8H_2O$, 99.99%) were provided by Shanghai McLean Co., Ltd. (McLean, Shanghai, China). Ammonia ($NH_3 \bullet H_2O$, 25%), hydrogen peroxide (H_2O_2, 30%), and anhydrous ethanol (C_2H_5OH) were purchased from XiLong Chemical Reagent Co., Ltd. (XiLong, Guangdong, China). CR was produced by the Chengdu Kelong Chemical Reagent Factory (Kelong, Chengdu, China). All the reagents mentioned above were of analytical grade.

2.2. Synthesis of Zr Doping of Nano-CeO_2 Nanoparticles

First, by adjusting the ratio of zirconium oxychloride to cerium nitrate and then adding deionised water as solvent, a 0.05 mol/L cerium nitrate solution with 50 mL Zr/(Zr + Ce) and molar ratio of 0% (1, 2, 3, 4, and 5%) was obtained. Subsequently, 0.005 mol of anionic surfactant sodium dodecyl benzene sulfonate (SDBS) was added to the cerium nitrate solution, which was magnetically stirred at 298 K until the surfactant and cerium nitrate were evenly mixed. We prepared 100 mL of 2 mol/L ammonia solution and used a peristaltic pump to extract cerium nitrate precursor solution at a constant speed and dropped it into the ammonia solution stirred at a high-speed using magnetic force. After the cerium nitrate drops were added, an appropriate amount of hydrogen peroxide was added to change the solution from purple to light yellow. The mixture was stirred for 30 min to complete the reaction. The samples were then centrifuged and washed alternately with deionised water and anhydrous ethanol until the washing liquid was neutral, dried in a vacuum oven at 333 K for 12 h, and then calcined at 773 K for 2 h. The dried powder was then grounded using an agate mortar. ZC0, ZC1, ZC2, ZC3, ZC4, and ZC5, representing Zr, were used to add CeO_2 nanoparticles in the proportions of 0, 1, 2, 3, 4, and 5%, respectively.

2.3. Characterization

The morphologies of the surfaces and cross-section of various Zr doping ratios of CeO_2 nanoparticles were observed via field-emission scanning electron microscopy (FE-SEM, Hitachi SU-70, Tokyo, Japan). Transmission electron microscope analysis (TEM, Hitachi H9500, Almelo, The Netherlands) for nano-CeO_2 was also performed. The surface elemental composition with various Zr doping ratios of nano-CeO_2 was examined using X-ray photoelectron spectroscopy (XPS, Thermo Scientific ESCALAB Xi+, Waltham, MA, USA).

Al-Kα radiation was used as the X-ray source, and the binding energies were referenced to the C 1s peak (284.8 eV). X-ray diffraction (XRD; Bruker-axs, San Jose, MA, USA) was conducted to characterise the particle size of the nanoadsorbent. CR adsorption capacity tests were performed to measure the absorption spectra using a UV-Vis spectrometer (UV-VIS, Puli TU-1901, Beijing, China). N_2 adsorption isotherms were measured at 77.3 K by using an automatic specific surface and micropore analyser (BET, BSD Instrument 3H-2000PM2, Beijing, China). Before the adsorption measurements, the nano-CeO_2 powders were degassed under flowing N_2 for 5 h at 393 K to remove any residual water and surface species. Raman spectra were used to analysis the Zr-doped CeO_2 nanocomposite material at room temperature using Horiba Raman system (Raman, HR Evolution, Montpellier, France) with a continuous wave laser operating at 532 nm.

2.4. Batch Adsorption Study

An aqueous stock solution of CR (500 mg/L) was prepared by dissolving CR in deionized water. The required concentration (100, 200, 300, and 400 mg/L) was obtained by continuous dilution with deionized water. A total of 100 mL each of CR dye solution with different concentrations were taken and 10 mg nano-CeO_2 adsorbent was added. To adjust the pH levels, solutions of 0.1 mol/L HCl and 0.1 mol/L NaOH were utilized. Then the solutions were stirred sufficiently with magnetic stirrer at 500 rpm in a neutral environment with a temperature of 298 K and a pH of 7. At different time intervals, 5 mL of suspension samples was taken for centrifugation separation, and the supernatant was collected to measure its absorbance at the maximum absorption wavelength of CR at 496 nm via UV-Vis spectrophotometry. All studies were conducted at pH of 7 except for the pH effect study. Equilibrium adsorption isotherms were studied at different initial concentrations (pH of 7). At different pH values (1–12), the CR removal efficiency was investigated at an initial concentration of 100 mg/L and an adsorption time of 120 min. Finally, all batch adsorption measurements were performed three times, and the average was used for the experiments. *The adsorption capacity Qe* (mg/g) and *removal rate* (%) by the CeO_2 nanoparticles were calculated using the formulae (1) and (2), respectively.

$$Adsorption\ capacity\ (Qe) = (\frac{V}{M}) \times (C_0 - C_f) \quad (1)$$

$$Removal\ (\%) = (1 - \frac{C_f}{C_0}) \times 100\% \quad (2)$$

where Qe is the equilibrium adsorption capacity (mg/g); C_0 and C_f are the initial and final concentrations of CR (mg/L), respectively; and V (L) and M (g) are the volume of the CR solution and adsorbent dosage, respectively.

3. Results

3.1. Phase Analysis

The X-ray diffraction patterns of cerium oxide and Zr^{4+}-doped cerium oxide revealed a crystal structure that aligns with the cubic fluorite structure of cerium oxide (PDF. 34–0394), as shown in Figure 1. The main characteristic peaks at 2θ = 28.6°, 33.0°, 47.5°, and 56.3° correspond to the crystal faces of (111), (200), (220), and (311) planes [35], respectively. The increase in the Zr doping content did not affect the positions of the four prominent peaks of CeO_2 in the XRD pattern. However, this resulted in a less-pronounced peak deformation and weakened peak intensity for CeO_2. This observation suggests that the characteristic peaks tend to weaken with increasing Zr doping concentration, indicating a decrease in the degree of sample crystallisation. The crystallite sizes of the ZC0, ZC1, ZC2, ZC3, ZC4, and ZC5 nanoparticles were 9.8, 9.0, 8.3, 7.1, 6.6, and 6.7 nm, respectively, as determined by the Scherrer formula (3) [36]. This analysis revealed a decreasing trend in grain size with increasing Zr doping ratio. These phenomena may be attributed to the doping of Zr into the CeO_2 lattice, which hindered the growth of the CeO_2 crystals. The reduction in

particle size suggests an increase in the surface adsorption of active sites of CeO_2, thereby enhancing its adsorption performance.

$$Crystallite\ Size = \frac{K_B\lambda}{\beta cos\theta} \quad (3)$$

where β, λ, and K_B are the full-width half maximum (FWHM), the wavelength of the X-ray (CuKα, λ = 0.154 nm), and the broadening constant (0.9), respectively.

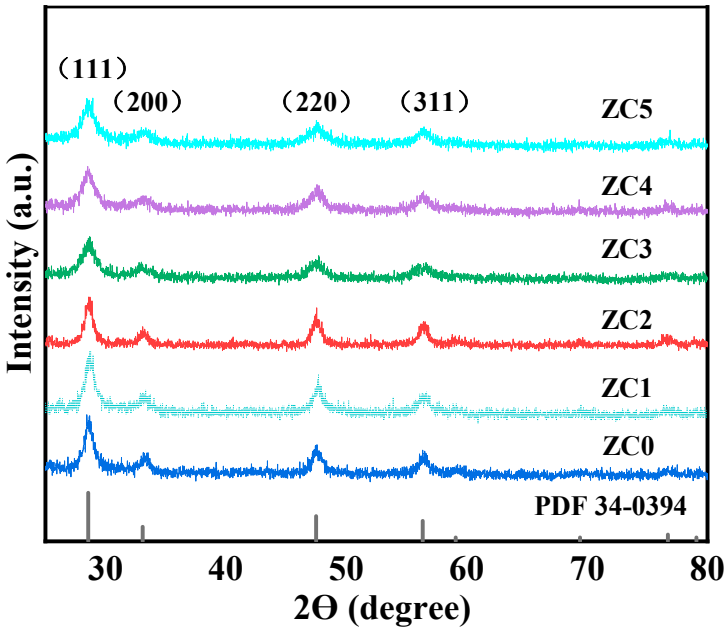


Figure 1. X-ray XRD diffraction pattern of CeO_2 doped with varying amounts of Zr.

3.2. SEM Analysis

Scanning electron microscopy (SEM) was employed to investigate the surface morphology of the pure cerium oxide ZC0 (a) and Zr-doped cerium oxides ZC1, ZC2, ZC3, ZC4, and ZC5 (b, c, d, e, and f, respectively), as shown in Figure 2. The results demonstrate that CeO_2 nanoparticles prepared by high-temperature calcination and doped with Zr exhibit a uniform particle size distribution. Compared to the undoped samples, the morphology of the CeO_2 nanoparticles remained largely unchanged, with a granular particle size distribution. Additionally, all samples exhibited a regular crystal structure which enhanced the adsorption process.

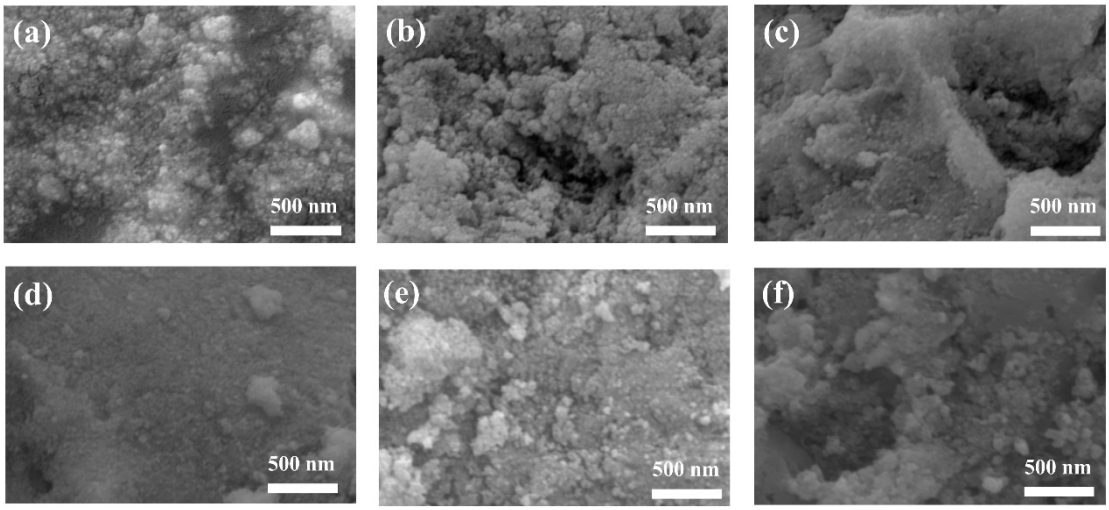


Figure 2. SEM images of (**a**) ZC0, (**b**) ZC1, (**c**) ZC2, (**d**) ZC3, (**e**) ZC4, and (**f**) ZC5 nanoparticles.

3.3. TEM Analysis

Figure 3 displays the TEM images and elemental distribution images of the nano-ZC3 particles doped with 3 atm% Zr at varying magnifications. As shown in Figure 3a, the Zr-doped nano-CeO_2, prepared through the co-precipitation of cerium nitrate and zirconium oxychloride with ammonia water, exhibited a distinct particle structure, indicating that the structure of the ZC3 nanoparticles remained unchanged after Zr doping while maintaining their nanoparticle form. At low magnification, the good dispersion of the ZC3 nanoparticles was observed using TEM. The average particle size was calculated to be 11.05 nm by the TEM image (a) statistics. Additionally, the elemental distribution diagram in Figure 3c demonstrates the uniform distribution of Zr, Ce, and O on the surface of the ZC3 nanoparticles.

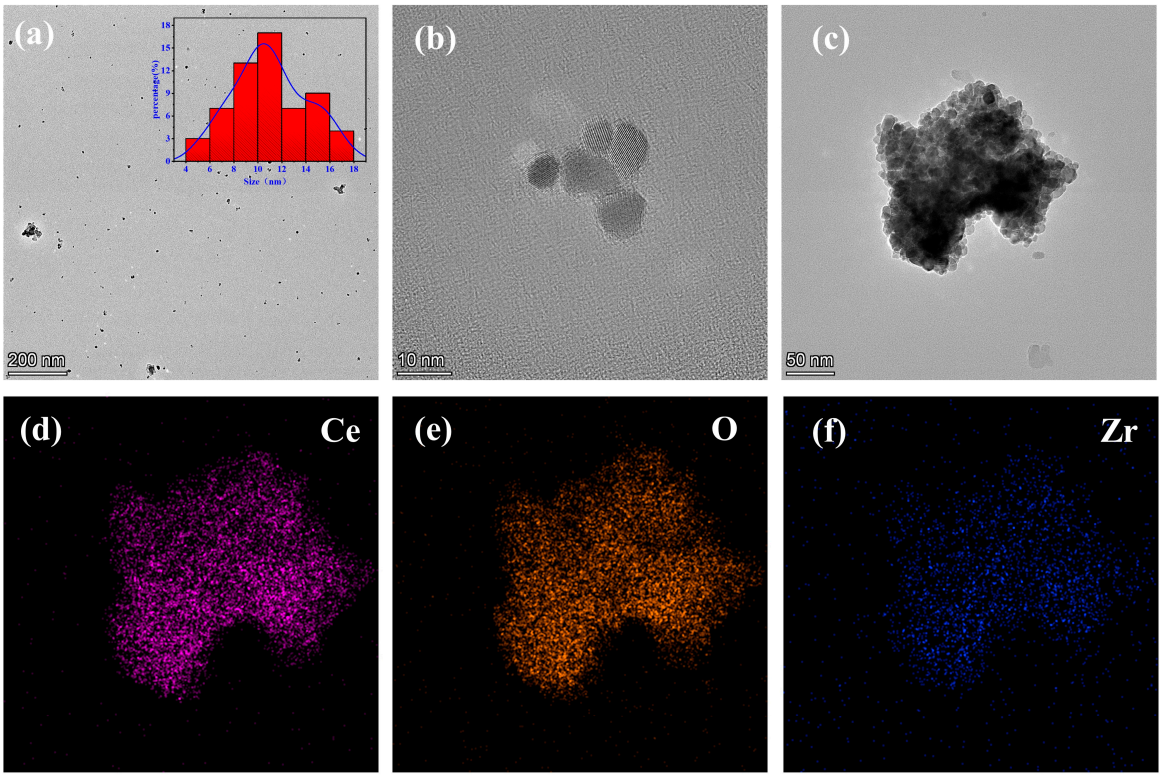


Figure 3. (**a**) Low-magnification TEM images of ZC3 nanoparticles; (**b**) High-magnification TEM images of ZC3 nanoparticles; (**c**) Image of element distribution of ZC3 nanoparticles; (**d**) The elemental distribution of Ce; (**e**) The elemental distribution of O; (**f**) The elemental distribution of Zr.

3.4. BET Analysis

The effect of the doping amount on the surface area was evaluated using nitrogen adsorption–desorption isotherms. As depicted in Figure 4, the ZC0, ZC1, ZC2, ZC3, ZC4, and ZC5 nanoparticles exhibit typical class IV isotherms and H2-type [37,38] hysteresis with a distinct jump observed at a relative pressure of $P/P_0 = 0.4$. These results indicated the presence of a mesoporous structure with a relatively uniform pore size distribution. The SEM and TEM analyses revealed that the formation of pore structures in the material primarily resulted from the aggregation of numerous nanoparticles, whereas interparticle pores facilitated adsorption. The specific surface areas of the ZC0, ZC1, ZC2, ZC3, ZC4, and ZC5 nanoparticles were 65.31, 73.90, 88.07, 82.38, 68.23 and 62.47 m^2/g, respectively. The specific surface areas and average pore diameters of the samples are listed in Table 1.

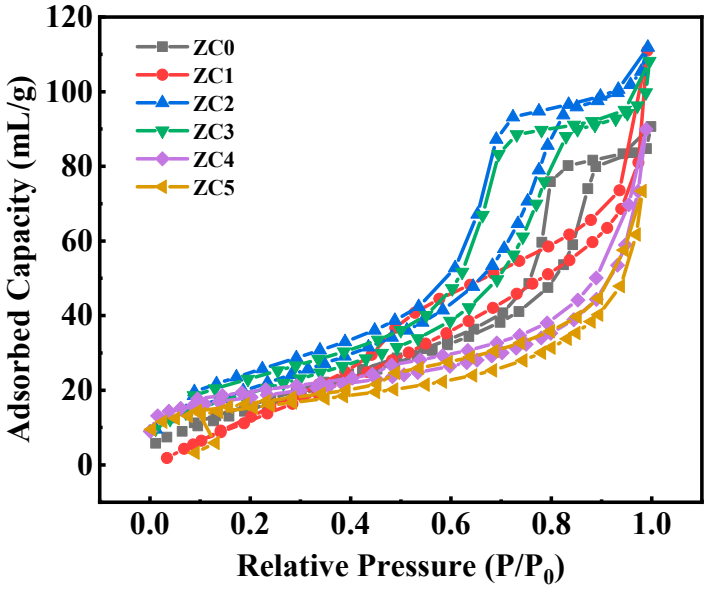


Figure 4. Nitrogen adsorption–desorption isotherm curves of Zr-doped CeO_2 nanoparticles.

Table 1. Specific surface area and average pore size of Zr-doped CeO_2 nanoparticles.

Sample	S_{BET} (m^2/g)	D_{BJH} (nm)
ZC0	65.31	8.05
ZC1	73.90	5.87
ZC2	88.07	6.76
ZC3	82.38	8.45
ZC4	68.23	9.08
ZC5	62.47	9.70

3.5. X-ray Photoelectron Spectroscopy

To further study the surface composition and chemical valence of the Zr-doped CeO_2 nanoparticles and determine whether Zr was successfully introduced into the CeO_2 nanoparticles, an XPS analysis was performed on the ZC0, ZC1, ZC2, ZC3, ZC4, and ZC5 nanoparticles. The full XPS spectrum of the Zr-doped CeO_2 nanoparticles, as depicted in Figure 5a, confirms the presence of characteristic peaks for Ce 3d, O 1s, C1s, and Zr 3d. This observation is consistent with the TEM mapping results and indicates the successful introduction of Zr into the CeO_2 nanoparticles. Figure 5b shows the Zr 3d spectra of the sample, where peg-split fitting was applied to the Zr 3d energy spectrum of ZC3 doped with 3% Zr. The binding energies at 182.4 and 185.6 eV [39] correspond to Zr 3d5/2 and Zr 3d3/2, respectively, suggesting the presence of surface-bound Zr^{4+} components in the ZC3 material [40,41].

The O 1s energy spectrum was fitted using Advantage software (5.918). The O 1s energy spectra of the undoped pure CeO_2 sample ZC0 and doped nanoparticles with 1~5% Zr, as depicted in Figure 6, were analysed using peak fitting to quantify the surface oxygen content of different types on the surface of CeO_2 particles with varying levels of Zr doping. The peak at approximately 530 eV [42] in the figure corresponds to the lattice oxygen (O_L) within the CeO_2 structure, whereas the peak at approximately 532 eV primarily represents surface vacancies (O_V) [43], and the peak near 533 eV indicates adsorbed oxygen on the surface (O_S). By calculating the ratio of peak areas, it can be determined that ZC3 nanoparticles possess an approximate oxygen vacancy content of 60.69%, which is significantly higher than that of undoped ZC0 (%). This demonstrates that doping with Zr^{4+} effectively reduces the lattice oxygen on the CeO_2 surface, resulting in a greater number of oxygen vacancies on ZC3 than on pure CeO_2. Based on these findings, it can be inferred that calcined samples with a 3% Zr doping content exhibit numerous adsorption sites for CR.

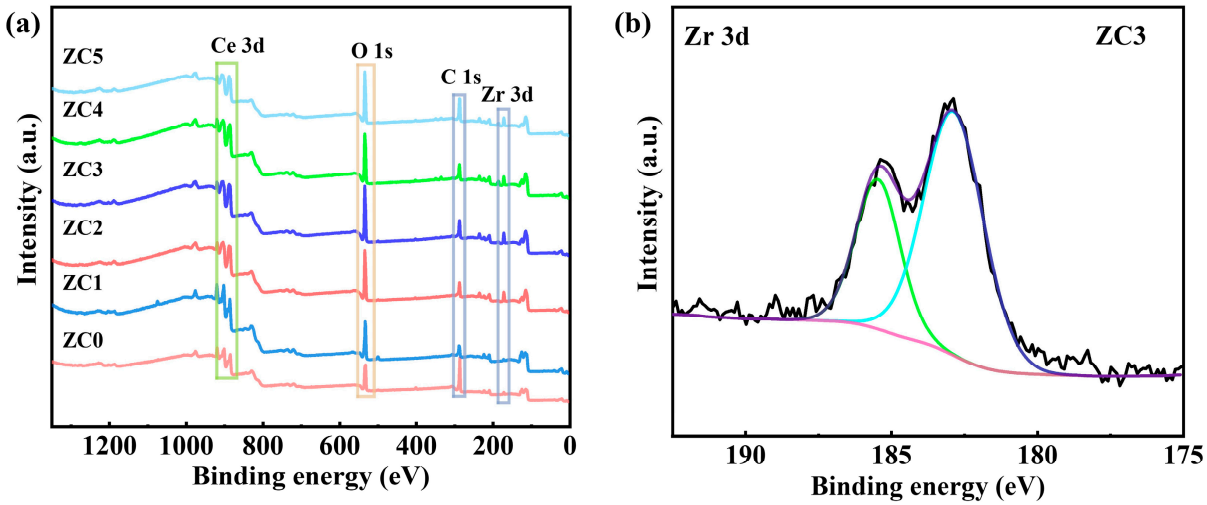


Figure 5. (**a**) Full XPS spectrum of Zr-doped CeO_2 nanoparticles; (**b**) Zr 3d fine spectrum of ZC3 (blue:182.4 eV; green:185.6 eV).

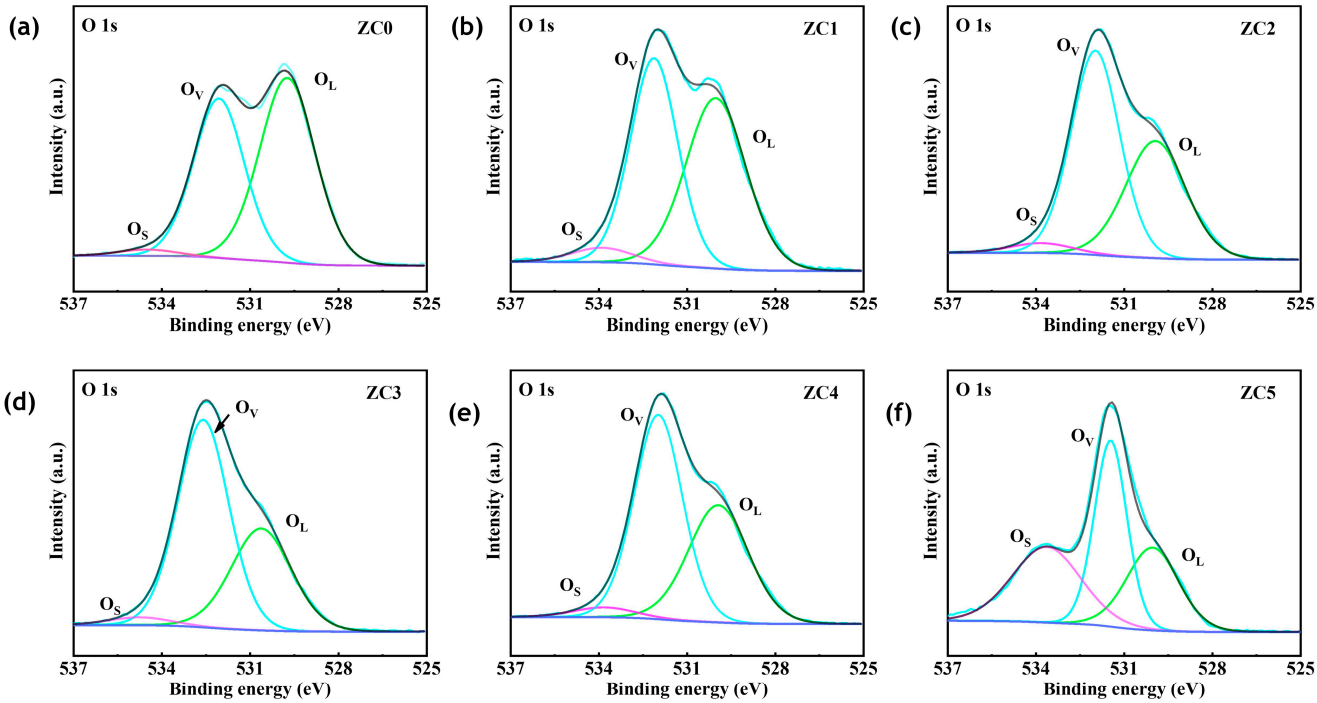


Figure 6. O 1s fine spectrum of Zr-doped CeO_2 (**a**) ZC0; (**b**) ZC1; (**c**) ZC2; (**d**) ZC3; (**e**) ZC4; (**f**) ZC5. (purple: O_S; blue: O_L; green: O_V).

From Table 2, it is evident that Zr doping induces a plethora of oxygen vacancies that are dependent on the degree of doping. If the doping level is extremely low, the lattice distortion will not be conspicuous, and the concentration of oxygen vacancies will remain low. Conversely, excessive doping impedes the diffusion of oxygen vacancies onto the sample surface, resulting in a decrease in their concentration. Therefore, an optimal threshold exists for CeO_2 to achieve the maximum oxygen vacancy content. In this system, CeO_2 attained its highest oxygen vacancy content (60.69%) when the Zr doping reached 3%.

Table 2. Content ratio of O_L, O_V, and O_S of Zr-doped CeO_2.

Sample	O_L%	O_V%	O_S%
ZC0	50.95	40.40	1.81
ZC1	50.92	41.25	4.08
ZC2	36.12	56.86	3.30
ZC3	34.86	60.69	2.64
ZC4	39.00	55.23	3.20
ZC5	27.20	40.12	36.28

3.6. Raman Analysis

The Raman spectra of the Zr-doped CeO_2 are presented in Figure 7. All spectra exhibit a main peak at n = 464 cm^{-1}, which could be assigned to the F_{2g} Raman-active mode of the fluorite-structured CeO_2. An additional small band at around n = 610 cm^{-1} is caused by the defects related to oxygen vacancies (O_v) [44–47]. No Raman bands that correspond to dopant oxides are detected, which is in agreement with the XRD results. Notably, the F_{2g} band of the Zr-doped CeO_2 is shifted to a lower wavenumber for relative to pure CeO_2. The shift in the F_{2g} mode reveals the variation in the M (metal)–O vibration frequency, which is attributed to the difference in the radii of Ce^{4+} and the dopants [44–46]. The difference in the ionic radius of the dopants enables changes in the lattice parameter caused by cell contraction or expansion. Hence, vibrations are stiffer in a contracted lattice and more relaxed in an expanded lattice so that the bands shift to higher and lower wavenumbers [48], respectively. Further, the incorporation of dopant ions into the CeO_2 changes the relative amount of oxygen vacancies (Figure 7, inset). The Zr-doped CeO_2 and pure CeO_2 samples exhibited only one type of O_v band at around n = 610 cm^{-1}. Generally, the extrinsic vacancies could be formed because of the oxygen vacancies introduced into the CeO_2 to maintain the charge neutrality if Ce^{4+} ions are replaced with trivalent cations [46,48], whereas the intrinsic vacancies are generated by the presence of Ce^{3+} ions. Therefore, the Zr-doped CeO_2 and pure CeO_2 promote only intrinsic vacancies attributed to the presence of Ce^{3+} ions in the samples.

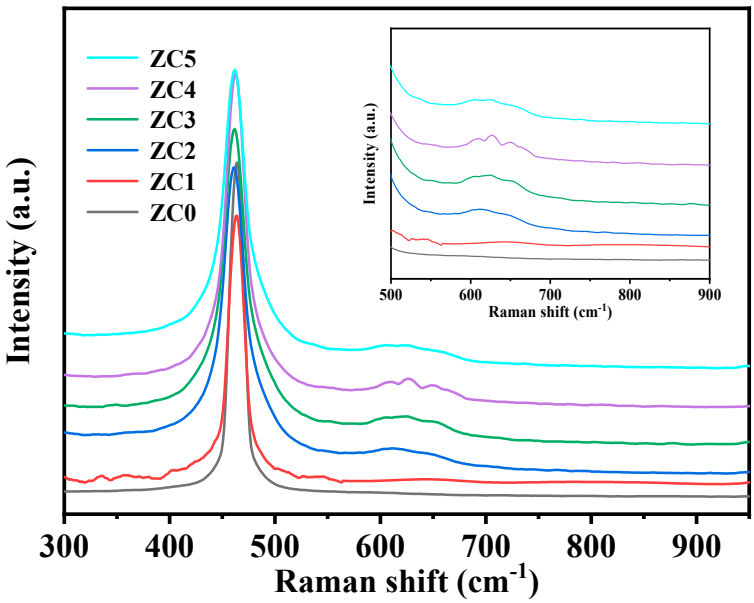


Figure 7. Raman spectra of Zr−doped CeO_2.

As the bands at n = 610 cm^{-1} are related to oxygen vacancies and the band at n = 464 cm^{-1} is the main band of the CeO_2-based samples, the area ratio of these bands $A(O_v)/A(F_{2g})$ (Figure 7, inset) reflects the relative concentration of oxygen vacancies. As a result, $A(O_v)/A(F_{2g})$ follows the sequence ZC3 > ZC2 > ZC4 > ZC5 > ZC1 > ZC0, which indicates that the ZC3 sample had the most defect sites and the ZC0 sample had the least,

which is consistent with the conclusions drawn from the results of the XPS. Notably, Raman spectroscopy is essentially a bulk technique. Therefore, the detected oxygen vacancies in the ceria and doped ceria samples are a sum of both the surface and bulk defects. As the particle sizes of all the samples here are small (~11 nm) and similar, it is reasonable to compare the relative amount of defect sites via Raman spectroscopy.

3.7. Adsorption of CR

3.7.1. Effect of Zr Doping Amount on Adsorption Properties

To compare the effect of the Zr doping ratio on the adsorption properties of CeO_2 nanoparticles, the adsorption properties of samples with different Zr doping levels were compared at room temperature with the other conditions remaining unchanged (the amount of adsorbent added was 10 mg, and the CR solution was 100 mg/L of 100 mL), as shown in Figure 8. The adsorption properties of CeO_2 prepared with different Zr doping ratios were significantly improved compared with those of undoped CeO_2 nanoparticles, which may be due to doping changes in its physical and chemical properties compared with those of pure CeO_2. Doping has a significant influence on the surface O_V of an adsorbent, and the surface O_V of vacant oxygen plays an important role in the adsorption process [27,49]. The interaction between the ammonium radical (NH_3^+) in CR and oxygen vacancy O_V determines the adsorption efficiency of the adsorbent [43,50,51]. The amount of vacant oxygen O_V may be affected by the amount of Zr doping [52]. The adsorption capacity of the nanoparticles with 3% Zr doping exhibited the best adsorption capacity, reaching 974 mg/g, whereas the adsorption performance of the undoped pure CeO_2 was only 787 mg/g.

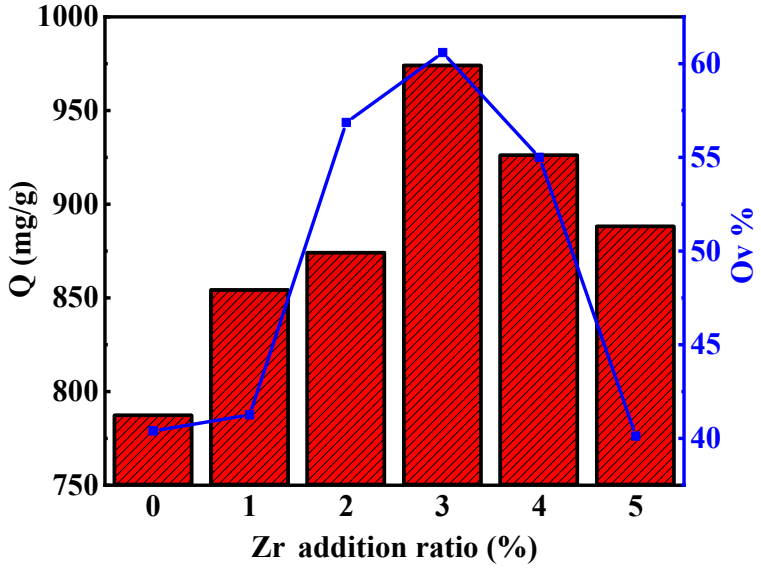


Figure 8. Influence of Zr doping levels on the adsorption properties of CeO_2 nanoparticles.

3.7.2. Effect of pH

The influence of pH on the CR adsorption performance was evaluated by changing the pH of the solution (pH = 1, 3, 5, 7, 9, 10, 11, and 12) at different initial pH values [50,53]. In this study, 0.01 g ZC3 particles were used to adsorb 100 mL of a 100 mg/L CR solution at different initial pH values, as shown in Figure 9. The influence of the pH on ZC0 is shown in Figure S1a. At pHs between 1 and 10, the removal of dyes was high, which can be attributed to the strong electrostatic interaction between the positively charged ZC3 nanoparticles and anionic CR (pH = 1–10) and the hydrogen bonding between the oxygen vacancy and the amino group of the CR molecules. At a higher pH (pH > 10), the significant decrease in the adsorption performance may have been attributed to the high pH neutralising the positive charge on the surface of the ZC3 nanoparticles, resulting in a negatively charged surface. Therefore, the anion of CR has a stronger repulsive effect on the negatively charged ZC3

nanoparticles, which leads to a reduction in the adsorption efficiency. However, because there are a large number of oxygen vacancies on the surface of the doped nanoparticles, which is also an important adsorption site for CR molecules, the increased pH can still maintain a certain adsorption performance. The pH (pH > 10) has a considerable effect on the adsorption efficiency, confirming that electrostatic interactions play an important role in the adsorption mechanism; the optimal pH value for adsorption studies was 7, which was used throughout the experiment. As the initial pH value increased from 7 to 12, the removal of CR gradually decreased, and the removal of ZC3 nanoparticles from the CR solution decreased from 98.7% to 44.6%. At a pH of >7, the adsorption performance of ZC3 was significantly better than that of ZC0, indicating that doping effectively improves the acid–base resistance of the adsorbent.

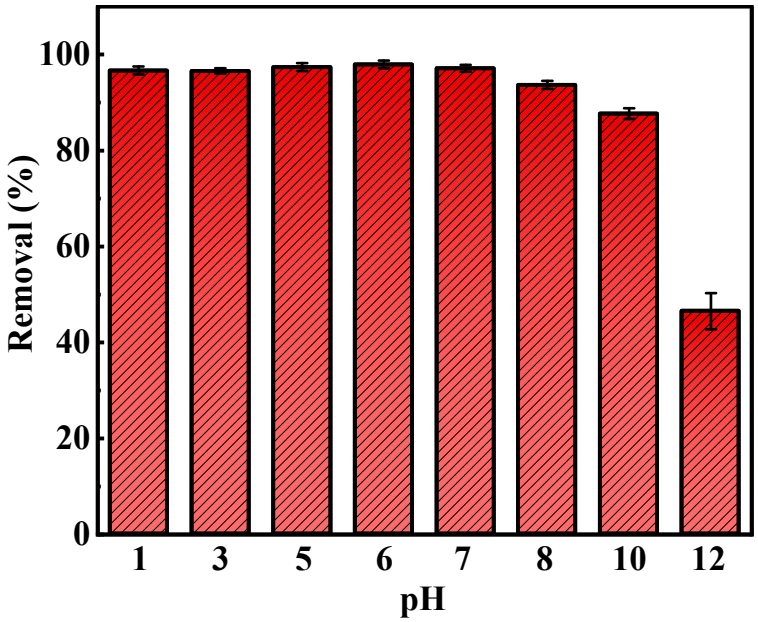


Figure 9. Influence of pH on the adsorption properties.

3.7.3. Effect of Contact Time

The change in the adsorption capacity of ZC3 nanoparticles on the CR solution over time is shown in Figure 10 and the effect of the contact time of ZC0 is shown in Figure S1b. There were a large number of vacancies on the surface of the nanoparticle adsorbent, which was conducive to improving the adsorption rate in the initial stage. BET data also confirmed the existence of a large number of mesoporous pores on the surface of ZC3 nanoparticles. Moreover, a high specific surface area of the ZC3 nanoparticle adsorbent ensured that there were sufficient vacancies for small dye molecules to reside in and interact with the adsorbent. Over time, the number of vacancies gradually decreases, owing to increased competition for active adsorption sites. Thus, during dye adsorption, a preliminary process involved the formation of a thin monolayer from the dispersed dye solution on the outer surface of the adsorbent. The CR molecules then diffused from the monolayer to the pores formed by the stacking of the adsorbent nanoparticles. Over time, the mesoporous pores in the adsorbent were filled. Ultimately, this provided resistance to the diffusion of the accumulated dye molecules onto the adsorbent. In this study, the amount of adsorbent was kept constant at 0.01 g/L. Therefore, for lower initial dye concentrations, the removal rate of the CR dye was higher and the time to reach the adsorption equilibrium was shorter. The CR adsorption dynamics included two phases. The first stage was the rapid adsorption stage, in which the adsorption (which may be instantaneous) was mainly on the outer surface. In the second stage, the adsorption gradually slowed. Finally, the adsorption of the two dyes reached an equilibrium. Considering these facts, for a lower initial concentration (100 mg/L), the time to reach an equilibrium was relatively less than that for a higher

initial concentration (400 mg/L). Therefore, a constant adsorption dose indicates a high adsorption rate. In the initial stage of the adsorption reaction, the adsorption capacity of the CR molecules on the ZC3 nanoparticles increased with increasing reaction time, and the rate of increase was significantly fast. After 30 min, the absorption rate stabilised.

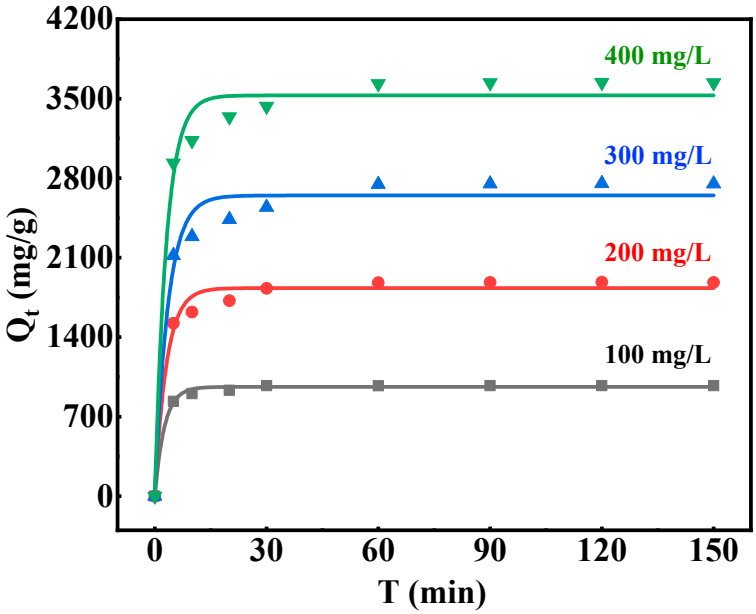


Figure 10. Effect of contact time (C_0 = 100~400 mg/L, pH = 7, temperature = 298 K, volume = 100 mL, dosage = 10 mg, and rpm = 500).

3.7.4. Adsorption Kinetics

Pseudo-first- and second-order kinetic models were used to fit the adsorption data. The linear expressions of the quasi-first- and second-order kinetic models are detailed in (4) and (5) [54–56], respectively. The adsorption data of the CR molecules by the ZC0 and ZC3 nanoparticles were fitted using pseudo-first- and second-order kinetic models, and the results are shown in Figures S1c,d and 11. The pseudo-second-order kinetic models' t/q_t with t exhibited a good linear relationship, as shown in Figures 11b and S1d. By calculating the fitting results, the parameters of the quasi-first- and second-order kinetic models were obtained [57], as presented in Table 3. The fitting results showed that the correlation coefficients R^2 of the quasi-second-order kinetic model for the molecular adsorption of CR by the ZC3 nanoparticles were 0.9932, 0.9966, 0.9967, and 0.9845. The equilibrium adsorption capacity fitted by the pseudo-second-order kinetic model was closer to the experimental results, indicating that the adsorption process of ZC3 nanoparticles on the CR molecules can be fitted by the quasi-second-order kinetic model. As listed in Table S1, the undoped ZC0 also conformed to pseudo-second-order kinetics, indicating chemisorption.

$$ln(q_e - q_t) = lnq_e - K_1 t \quad (4)$$

$$\frac{t}{q_t} = \frac{1}{K_2 q_e^2} + \frac{1}{q_e} t \quad (5)$$

Here, *qe* is the CR adsorption capacity at the time of equilibrium, while q_t is related to the CR adsorption capacity at time *t*; K_1 is the kinetic rate constant when applying the pseudo-first-order reaction (min^{-1}) using the prepared materials of ZC3; and K_2 is the rate constant of the pseudo-second-order reaction ($g/mg^{-1}{\cdot}min^{-1}$).

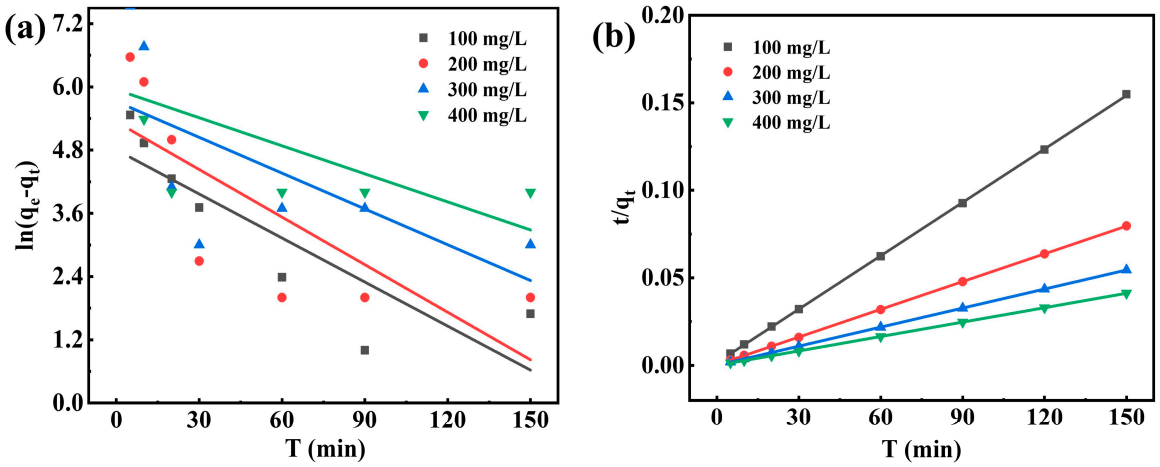


Figure 11. (**a**) Pseudo−first−order reaction; (**b**) pseudo−second−order reaction.

Table 3. Kinetic parameters for the adsorption of the CR onto ZC3.

C_0 (mg/L)	q_e, exp (mg/g)	Pseudo-First-Order			Pseudo-Second-Order		
		K_1	q_e	R^2	K_2	q_e	R^2
100	974.31	0.02786	121.51	0.751	6.50×10^{-4}	980.39	0.9994
200	1884.23	0.03010	207.30	0.594	8.18×10^{-4}	1893.08	0.9997
300	2753.61	0.02265	305.46	0.421	12.48×10^{-4}	2758.39	0.9999
400	3642.05	0.01775	382.58	0.329	29.56×10^{-4}	3644.31	0.9999

3.7.5. Adsorption Isotherm

The adsorption properties of the ZC0 and ZC3 nanoparticles for the CR at 298 K were studied. The Langmuir (6) and Freundlich (7) isothermal absorption models [58,59] were used to fit the experimental data for the adsorption of CR on the Zc0 and ZC3 particles, and the results are shown in Figure S1e,f and 12. As summarized in Tables 4 and S2, the correlation coefficients R^2 of the Langmuir and Freundlich models were both greater than 0.9; however, the fitting effect of the Freundlich model was better, indicating that the adsorption process of Zr-doped CeO_2 nanoparticles on CR may be a combination of physical adsorption and chemisorption. Physical adsorption is caused by electrostatic attraction, and chemisorption is caused by the interaction between surface oxygen vacancies and dye molecules. A zeta potential analysis was performed on ZC0, ZC3, and CR dyes, as shown in Figure S2. The CR dyes were negatively charged, whereas ZC0 and ZC3 were positively charged. The ZC3 potential increased after doping. A comparison of the adsorption properties with those of other materials is presented in Table S3.

$$\frac{C_e}{q_e} = \frac{1}{q_m b} + \frac{C_e}{q_m} \tag{6}$$

$$lnq_e = lnK_f + \frac{lnC_e}{n} \tag{7}$$

where q_m was the theoretical maximum adsorption capacity of the adsorbent (mg/g); b is one of the important parameters of the Langmuir isotherm adsorption model (L/mg); Ce is the adsorption equilibrium of the solution concentration (mg/L); q_e is the unit mass of the adsorbent adsorption capacity (mg/g); and K_f and $1/n$ are related to the adsorption capacity and adsorption intensity of the Freundlich isothermal adsorption model parameters.

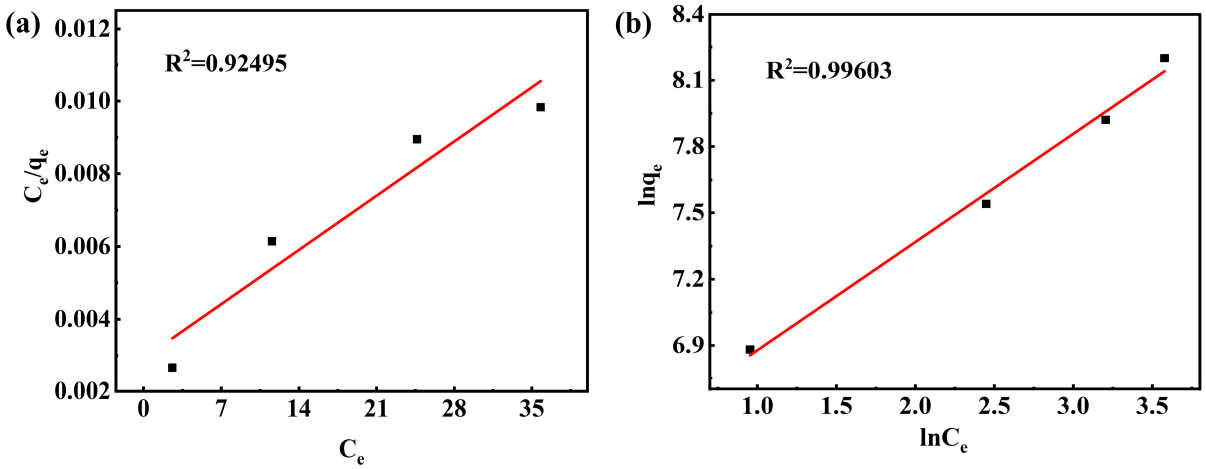


Figure 12. (**a**) Langmuir; (**b**) Freundlich. (C_0 = 100~400 mg/L, pH = 7, temperature = 298 K, volume = 100 mL, dosage = 10 mg, and rpm = 500).

Table 4. Isothermal adsorption model of CR molecules on ZC3.

T(K)	Langmuir Isotherm			Freundlich Isotherm		
	q_m	b	R^2	K_f	1/n	R^2
298	3642.05	1.2893	0.92495	544.57	0.4899	0.99603

From Table 5, we can see that the adsorption capacity and removal rate of adsorbent are affected by the amount of adsorbent added and the concentration of the dye. The ZC3 anionic dye prepared by this study still has an excellent adsorption performance when there is a high concentration of dye wastewater, and only a small amount of adsorbent is needed to remove the Congo red anionic dye.

Table 5. Various recent reports on the CeO_2- and Zr-doped CeO_2 for pigmented anionic dye adsorption.

Adsorbents	Dyes	Dosages (g)	Concentrations	q_e (mg/g)	Removal (%)	Ref.
$CeO_2 \cdot xH_2O$	AR14	0.04	40 mL, 250 mg/L	540	/	[50]
CeO_2 nanospheres	CR	0.005	50 mL, 100 mg/L	942.7	94.27	[60]
Spindle CeO_2	CR	0.05	50 mL, 200 mg/L	162.4	81.2	[61]
$Ce_xZr_{1-x}O_2$ solid solution	MO	0.06	40 mL, 40 mg/L	21.7	82.2	[62]
ZC0	CR	0.01	100 mL, 200 mg/L	1289.49	64.47	This work
ZC3	CR	0.01	100 mL, 400 mg/L	3642.05	91.05	This work

4. Conclusions

Based on a study on the adsorption process of CR dye, CeO_2 nanoparticles synthesised with a 3% Zr doping ratio demonstrated the highest adsorption capacity for CR. These nanoparticles exhibit an excellent adsorption performance across a wide pH range and achieved a maximum adsorption capacity of 3642.05 mg/g at room temperature. The adsorption process followed a quasi-second-order kinetic model, and the isothermal data were consistent with both the Langmuir and Freundlich models. The XPS analysis of different doping ratios of nano-CeO_2 combined with CR in the adsorption experiments revealed that oxygen vacancies on the CeO_2 surface significantly influenced the adsorption performance of CR and may serve as primary active sites for adsorption. In conclusion, Zr-doped CeO_2 nanoparticles have significant potential for the development of and applications for the effective removal of anionic dyes from wastewater because of their straightforward preparation methods and exceptional adsorptive properties.

Supplementary Materials: The following supporting information can be downloaded at: https://www.mdpi.com/article/10.3390/cryst13121641/s1, Figure S1: Performance of ZC0 at different pH (a), the effect of contact time. (b), Pseudo-first adsorption model (c), Pseudo-second adsorption model (d), Langmuir (e), Freundlich (f); Figure S2: Dispersion of zeta potential in a neutral aqueous environment for CeO2, ZC3 nanoparticles, and CR; Table S1: Kinetic parameters for the adsorption of Congo Red on ZC0; Table S2: Isothermal adsorption model of CR molecules on ZC0; Table S3. Comparison of adsorption performance in this study with previous Congo red dye adsorbent in works in the literature. References [63–72] have been explained in the Supplementary Materials.

Author Contributions: N.L. and Y.C. conceived the study and designed the experiments. N.L. and L.F. performed the experiments. N.L. wrote the article. W.L. revised the article. All authors have read and agreed to the published version of the manuscript.

Funding: This research received no external funding.

Data Availability Statement: Data are contained within the article and Supplementary Materials.

Acknowledgments: This work was supported by Suntar Membrane Technology (Xiamen) Co., Ltd., Xiamen.

Conflicts of Interest: Authors YunQiang Chen and Lei Fan were employed by the company Suntar Membrane Technology (Xiamen) Co., Ltd., the remaining authors declare that the research was conducted in the absence of any commercial or financial relationships that could be construed as a potential conflict of interest.

References

1. Liu, Z.; Zhang, J.; Zhang, L.; Guan, Y.; Ji, H.; Zhang, Y.; Gao, H. Efficient removal of Congo red and methylene blue using biochar from Medulla Tetrapanacis modified by potassium carbonate. *Bioresour. Technol.* **2023**, *376*, 128912. [CrossRef] [PubMed]
2. Praveen, S.; Jegan, J.; Bhagavathi Pushpa, T.; Gokulan, R.; Bulgariu, L. Biochar for removal of dyes in contaminated water: An overview. *Biochar* **2022**, *4*, 10. [CrossRef]
3. Liu, Z.; Hu, Y.; Zhang, J.; Guan, Y.; Zhang, L.; Ye, P.; Zhang, T.; Huang, X.; Wang, M.; Gao, H. Enhanced adsorption of Congo red from urea/calcium chloride co-modified biochar: Performance, mechanisms and toxicity assessment. *Bioresour. Technol.* **2023**, *388*, 129783. [CrossRef] [PubMed]
4. Cho, S.-H.; Jung, S.; Park, J.; Lee, S.; Kim, Y.; Lee, J.; Fai Tsang, Y.; Kwon, E.E. Strategic use of crop residue biochars for removal of hazardous compounds in wastewater. *Bioresour. Technol.* **2023**, *387*, 129658. [CrossRef] [PubMed]
5. Kloster, G.A.; Mosiewicki, M.A.; Marcovich, N.E. Chitosan/iron oxide nanocomposite films: Effect of the composition and preparation methods on the adsorption of congo red. *Carbohydr. Polym.* **2019**, *221*, 186–194. [CrossRef] [PubMed]
6. Zheng, Y.; Cheng, B.; Fan, J.; Yu, J.; Ho, W. Review on nickel-based adsorption materials for Congo red. *J. Hazard. Mater.* **2021**, *403*, 123559. [CrossRef]
7. Poornima, P.V.; Parimaladevi, R.; Sathe, V.; Mahalingam, U. Graphene boosted silver nanoparticles as surface enhanced Raman spectroscopic sensors and photocatalysts for removal of standard and industrial dye contaminants. *Sens. Actuat. B* **2019**, *281*, 679–688. [CrossRef]
8. Shaban, M.; Abukhadra, M.R.; Shahien, M.G.; Ibrahim, S.S. Novel bentonite/zeolite-NaP composite efficiently removes methylene blue and Congo red dyes. *Environ. Chem. Lett.* **2018**, *16*, 275–280. [CrossRef]
9. Hussain, Z.; Chang, N.; Sun, J.; Xiang, S.; Ayaz, T.; Zhang, H.; Wang, H. Modification of coal fly ash and its use as low-cost adsorbent for the removal of directive, acid and reactive dyes. *J. Hazard. Mater.* **2022**, *422*, 126778. [CrossRef]
10. Tochetto, G.A.; Simão, L.; de Oliveira, D.; Hotza, D.; Immich, A.P.S. Porous geopolymers as dye adsorbents: Review and perspectives. *J. Clean. Prod.* **2022**, *374*, 133982. [CrossRef]
11. Liu, J.; Wang, Z.; Li, H.; Hu, C.; Raymer, P.; Huang, Q. Effect of solid state fermentation of peanut shell on its dye adsorption performance. *Bioresour. Technol.* **2018**, *249*, 307–314. [CrossRef] [PubMed]
12. Stanciu, M.C.; Nichifor, M. Influence of dextran hydrogel characteristics on adsorption capacity for anionic dyes. *Carbohydr. Polym.* **2018**, *199*, 75–83. [CrossRef] [PubMed]
13. Yan, S.; Pan, Y.; Wang, L.; Liu, J.; Zhang, Z.; Huo, W.; Yang, J.; Huang, Y. Synthesis of low-cost porous ceramic microspheres from waste gangue for dye adsorption. *J. Adv. Ceram.* **2018**, *7*, 30–40. [CrossRef]
14. Panchu, S.E.; Sekar, S.; Kolanthai, E.; Sridharan, M.B.; Subbaraya, N.K. Extremely fast and efficient removal of Congo Red using cationic-incorporated hydroxyapatite nanoparticles (HAp: X (X = Fe, Ni, Zn, Co, and Ag)). *Crystals* **2023**, *13*, 209. [CrossRef]
15. Schmitt, R.; Nenning, A.; Kraynis, O.; Korobko, R.; Frenkel, A.I.; Lubomirsky, I.; Haile, S.M.; Rupp, J.L.M. A review of defect structure and chemistry in ceria and its solid solutions. *Chem. Soc. Rev.* **2020**, *49*, 554–592. [CrossRef]
16. Kim, Y.G.; Lee, Y.; Lee, N.; Soh, M.; Kim, D.; Hyeon, T. Ceria-based therapeutic antioxidants for biomedical applications. *Adv. Mater.* **2022**, *10*, 819. [CrossRef] [PubMed]

17. Olivera, S.; Chaitra, K.; Venkatesh, K.; Muralidhara, H.B.; Inamuddin; Asiri, A.M.; Ahamed, M.I. Cerium dioxide and composites for the removal of toxic metal ions. *Environ. Chem. Lett.* **2018**, *16*, 1233–1246. [CrossRef]
18. Gupta, K.; Joshi, P.; Gusain, R.; Khatri, O.P. Recent advances in adsorptive removal of heavy metal and metalloid ions by metal oxide-based nanomaterials. *Coord. Chem. Rev.* **2021**, *445*, 214100. [CrossRef]
19. Mallakpour, S.; Radfar, Z.; Feiz, M. Chitosan/tannic acid/ZnFe layered double hydroxides and mixed metal oxides nanocomposite for the adsorption of reactive dyes. *Carbohydr. Polym.* **2023**, *305*, 120528. [CrossRef]
20. Gusain, R.; Gupta, K.; Joshi, P.; Khatri, O.P. Adsorptive removal and photocatalytic degradation of organic pollutants using metal oxides and their composites: A comprehensive review. *Adv. Colloid Interface Sci.* **2019**, *272*, 102009. [CrossRef]
21. Suresh Kumar, P.; Korving, L.; Keesman, K.J.; van Loosdrecht, M.C.M.; Witkamp, G.-J. Effect of pore size distribution and particle size of porous metal oxides on phosphate adsorption capacity and kinetics. *Chem. Eng. J.* **2019**, *358*, 160–169. [CrossRef]
22. Xiao, W.; Garba, Z.N.; Sun, S.; Lawan, I.; Wang, L.; Lin, M.; Yuan, Z. Preparation and evaluation of an effective activated carbon from white sugar for the adsorption of rhodamine B dye. *J. Clean. Prod.* **2020**, *253*, 119989. [CrossRef]
23. Zhang, Y.; Wang, P.; Hussain, Z.; Zhang, H.; Wang, H.; Chang, N.; Li, F. Modification and characterization of hydrogel beads and its used as environmentally friendly adsorbent for the removal of reactive dyes. *J. Clean. Prod.* **2022**, *342*, 130789. [CrossRef]
24. Sachin; Singh, N.; Shah, K.; Pramanik, B.K. Synthesis and application of manganese-doped zinc oxide as a potential adsorbent for removal of Congo red dye from wastewater. *Environ. Res.* **2023**, *233*, 116484. [CrossRef] [PubMed]
25. Yahyaei, B.; Azizian, S. Rapid adsorption of anionic dyes by ordered nanoporous alumina. *Chem. Eng. J.* **2012**, *209*, 589–596. [CrossRef]
26. Sun, C.; Li, H.; Chen, L. Nanostructured ceria-based materials: Synthesis, properties, and applications. *Energy Environ. Sci.* **2012**, *5*, 8475–8505. [CrossRef]
27. Zhao, S.; Wen, Y.; Du, C.; Tang, T.; Kang, D. Introduction of vacancy capture mechanism into defective alumina microspheres for enhanced adsorption of organic dyes. *Chem. Eng. J.* **2020**, *402*, 126180. [CrossRef]
28. Thangamani, K.S.; Muthulakshmi Andal, N.; Ranjith Kumar, E.; Saravanabhavan, M. Utilization of magnetic nano cobalt ferrite doped Capra aegagrus hircus dung activated carbon composite for the adsorption of anionic dyes. *J. Environ. Chem. Eng.* **2017**, *5*, 2820–2829. [CrossRef]
29. Joshy, D.; Chakko, S.; Ismail, Y.A.; Periyat, P. Surface basicity mediated rapid and selective adsorptive removal of Congo red over nanocrystalline mesoporous CeO_2. *Nanoscale Adv.* **2021**, *3*, 6704–6718. [CrossRef]
30. Su, Y.-Q.; Zhang, L.; Muravev, V.; Hensen, E.J.M. Lattice oxygen activation in transition metal doped ceria. *Chin. J. Catal.* **2020**, *41*, 977–984. [CrossRef]
31. Mei, Z.; Li, Y.; Fan, M.; Zhao, L.; Zhao, J. Effect of the interactions between Pt species and ceria on Pt/ceria catalysts for water gas shift: The XPS studies. *Chem. Eng. J.* **2015**, *259*, 293–302. [CrossRef]
32. Massardo, S.; Pani, M.; Carnasciali, M.M.; Presto, S.; Viviani, M.; Artini, C. Defect chemistry of (Nd,Tm)- and (Nd,Dy)-doped ceria as revealed by Raman and electrochemical impedance spectroscopy. *Solid State Ion.* **2023**, *403*, 116403. [CrossRef]
33. Yatoo, M.A.; Skinner, S.J. Oxygen transport in higher-order ruddlesden-popper phase materials. *ECS Trans.* **2023**, *111*, 2405. [CrossRef]
34. Yatoo, M.A.; Seymour, I.D.; Skinner, S.J. Neutron diffraction and DFT studies of oxygen defect and transport in higher-order Ruddlesden–Popper phase materials. *RSC. Adv.* **2023**, *13*, 13786–13797. [CrossRef] [PubMed]
35. Phoka, S.; Laokul, P.; Swatsitang, E.; Promarak, V.; Seraphin, S.; Maensiri, S. Synthesis, structural and optical properties of CeO_2 nanoparticles synthesized by a simple polyvinyl pyrrolidone (PVP) solution route. *Mater. Chem. Phys.* **2009**, *115*, 423–428. [CrossRef]
36. Kumaresan, N.; Ramamurthi, K.; Ramesh Babu, R.; Sethuraman, K.; Moorthy Babu, S. Hydrothermally grown ZnO nanoparticles for effective photocatalytic activity. *Appl. Surf. Sci.* **2017**, *418*, 138–146. [CrossRef]
37. Ranjan, P.; Kumar, L.S.; Suematsu, H.; Chakravarthy, S.R.; Jayaganthan, R.; Sarathi, R. Thermodynamic analysis of ZnO nanoparticle formation by wire explosion process and characterization. *Ceram. Int.* **2017**, *43*, 6709–6720. [CrossRef]
38. Piumetti, M.; van der Linden, B.; Makkee, M.; Miceli, P.; Fino, D.; Russo, N.; Bensaid, S. Contact dynamics for a solid–solid reaction mediated by gas-phase oxygen: Study on the soot oxidation over ceria-based catalysts. *Appl. Catal. B* **2016**, *199*, 96–107. [CrossRef]
39. Zhang, F.; Liu, Z.; Chen, X.; Rui, N.; Betancourt, L.E.; Lin, L.; Xu, W.; Sun, C.-j.; Abeykoon, A.M.M.; Rodriguez, J.A.; et al. Effects of Zr doping into ceria for the dry reforming of methane over $Ni/CeZrO_2$ catalysts: In situ studies with XRD, XAFS, and AP-XPS. *ACS Catal.* **2020**, *10*, 3274–3284. [CrossRef]
40. Sun, M.; Li, Z.; Li, H.; Wu, Z.; Shen, W.; Fu, Y.Q. Mesoporous Zr-doped CeO_2 nanostructures as superior supercapacitor electrode with significantly enhanced specific capacity and excellent cycling stability. *Electrochim. Acta* **2020**, *331*, 135366. [CrossRef]
41. Zhao, H.; Dong, Y.; Jiang, P.; Wang, G.; Zhang, J. Highly dispersed CeO_2 on TiO_2 nanotube: A synergistic nanocomposite with superior peroxidase-like activity. *ACS. Appl. Mater. Int.* **2015**, *7*, 6451–6461. [CrossRef] [PubMed]
42. Janoš, P.; Hladík, T.; Kormunda, M.; Ederer, J.; Šťastný, M. Thermal treatment of cerium oxide and its properties: Adsorption ability versus degradation efficiency. *Adv. Mater. Sci. Eng.* **2014**, *2014*, 706041. [CrossRef]
43. Ma, F.; Yao, J.; Zhang, Y.; Wei, Y. Oxygen vacancy promoting adsorption property of BiOI microspheres modified with SDS. *Chin. Chem. Lett.* **2018**, *29*, 1689–1691. [CrossRef]

44. Yao, X.; Yu, Q.; Ji, Z.; Lv, Y.; Cao, Y.; Tang, C.; Gao, F.; Dong, L.; Chen, Y. A comparative study of different doped metal cations on the reduction, adsorption and activity of $CuO/Ce_{0.67}M_{0.33}O_2$ ($M=Zr^{4+}$, Sn^{4+}, Ti^{4+}) catalysts for NO+CO reaction. *Appl. Catal. B* **2013**, *130–131*, 293–304. [CrossRef]
45. Prasad, D.H.; Park, S.Y.; Ji, H.I.; Kim, H.R.; Son, J.W.; Kim, B.K.; Lee, H.W.; Lee, J.H. Structural characterization and catalytic activity of $Ce_{0.65}Zr_{0.25}RE_{0.1}O_{2-\delta}$ nanocrystalline powders synthesized by the glycine-nitrate process. *J. Phy. Chem. C* **2012**, *116*, 3467–3476. [CrossRef]
46. Sudarsanam, P.; Mallesham, B.; Reddy, P.S.; Großmann, D.; Grünert, W.; Reddy, B.M. Nano-Au/CeO_2 catalysts for CO oxidation: Influence of dopants (Fe, La and Zr) on the physicochemical properties and catalytic activity. *Appl. Catal. B* **2014**, *144*, 900–908. [CrossRef]
47. Wu, Z.; Li, M.; Howe, J.; Meyer, H.M., III; Overbury, S.H. Probing defect sites on CeO_2 nanocrystals with well-defined surface planes by Raman spectroscopy and O_2 adsorption. *Langmuir* **2010**, *26*, 16595–16606. [CrossRef]
48. Li, M.; Tumuluri, U.; Wu, Z.; Dai, S. Effect of dopants on the adsorption of carbon dioxide on ceria surfaces. *ChemSusChem* **2015**, *8*, 3651–3660. [CrossRef]
49. Cao, N.; Zhao, X.; Gao, M.; Li, Z.; Ding, X.; Li, C.; Liu, K.; Du, X.; Li, W.; Feng, J.; et al. Superior selective adsorption of MgO with abundant oxygen vacancies to removal and recycle reactive dyes. *Sep. Purif. Technol.* **2021**, *275*, 119236. [CrossRef]
50. Wang, H.; Zhong, Y.; Yu, H.; Aprea, P.; Hao, S. High-efficiency adsorption for acid dyes over $CeO_2 \cdot xH_2O$ synthesized by a facile method. *J. Alloys Compd.* **2019**, *776*, 96–104. [CrossRef]
51. Ren, P.; Ren, X.; Xu, J.; Li, H.; Zheng, Y.; Hong, Y.; Lin, Y.; Zhou, Y.; Chen, Y.; Zhang, W. Excellent adsorption property and mechanism of oxygen vacancies-assisted hexagonal MoO_3 nanosheets for methylene blue and rhodamine b dyes. *Appl. Surf. Sci.* **2022**, *597*, 153699. [CrossRef]
52. Zhang, S.; Yang, H.; Huang, H.; Gao, H.; Wang, X.; Cao, R.; Li, J.; Xu, X.; Wang, X. Unexpected ultrafast and high adsorption capacity of oxygen vacancy-rich WO_x/C nanowire networks for aqueous Pb^{2+} and methylene blue removal. *J. Mater. Chem. A* **2017**, *5*, 15913–15922. [CrossRef]
53. Wang, R.; Liu, L.; Subhan, S.; Muhammad, Y.; Hu, Y.; Huang, M.; Peng, Y.; Zhao, Z.; Zhao, Z. Engineering pH-switchable UiO-66 via in-situ amino acid doping for highly selective adsorption of anionic dyes. *Chem. Eng. J.* **2020**, *395*, 124958. [CrossRef]
54. Wu, F.-C.; Tseng, R.-L.; Juang, R.-S. Kinetic modeling of liquid-phase adsorption of reactive dyes and metal ions on chitosan. *Water. Res.* **2001**, *35*, 613–618. [CrossRef]
55. Liu, Z.; He, X.; Yang, X.; Ding, H.; Wang, D.; Ma, D.; Feng, Q. Synthesis of mesoporous carbon nitride by molten salt-assisted silica aerogel for Rhodamine B adsorption and photocatalytic degradation. *J. Mater. Sci.* **2021**, *56*, 11248–11265. [CrossRef]
56. Nayak, B.; Samant, A.; Patel, R.; Misra, P.K. Comprehensive understanding of the kinetics and mechanism of fluoride removal over a potent nanocrystalline hydroxyapatite surface. *ACS Omega* **2017**, *2*, 8118–8128. [CrossRef]
57. Mutahir, S.; Yaqoob, F.; Khan, M.A.; Alsuhaibani, A.M.; Abouzied, A.S.; Refat, M.S.; Huwaimel, B. Schiff-based modified bentonite clay composites for wastewater treatment: Experimental and DFT-based analysis. *Crystals* **2023**, *13*, 806. [CrossRef]
58. Ghaedi, M.; Biyareh, M.N.; Kokhdan, S.N.; Shamsaldini, S.; Sahraei, R.; Daneshfar, A.; Shahriyar, S. Comparison of the efficiency of palladium and silver nanoparticles loaded on activated carbon and zinc oxide nanorods loaded on activated carbon as new adsorbents for removal of Congo red from aqueous solution: Kinetic and isotherm study. *Mater. Sci. Eng. C* **2012**, *32*, 725–734. [CrossRef]
59. Su, Y.; Cui, M.; Zhu, J.; Wu, Y.; Wei, Y.; Bian, S. A facile synthesis of nanosheet-structured barium carbonate spheres with a superior adsorption capacity for Cr(VI) removal. *J. Mater. Sci.* **2018**, *53*, 4078–4088. [CrossRef]
60. Ouyang, X.; Li, W.; Xie, S.; Zhai, T.; Yu, M.; Gan, J.; Lu, X. Hierarchical CeO_2 nanospheres as highly-efficient adsorbents for dye removal. *New J. Chem.* **2013**, *37*, 585–588. [CrossRef]
61. Zheng, N.-C.; Wang, Z.; Long, J.-Y.; Kong, L.-J.; Chen, D.-Y.; Liu, Z.-Q. Shape-dependent adsorption of CeO_2 nanostructures for superior organic dye removal. *J. Colloid Interface Sci.* **2018**, *525*, 225–233. [CrossRef]
62. Bao, H.; Qian, K.; Chen, X.; Fang, J.; Huang, W. Spectroscopic study of microstructure-reducibility relation of $Ce_xZr_{1-x}O_2$ solid solutions. *Appl. Surf. Sci.* **2019**, *467–468*, 361–369. [CrossRef]
63. Bello, O.S.; Akinwale, F.T.; Agboola, O.S.; Ibrahim, A.O.; Adesina, O.O. Liquid-phase adsorption of Congo red dye using modified spear grass (*Imperata cylindrica*) root as adsorbent. *Biomass Convers. Biorefin.* **2022**, *2190*, 6823. [CrossRef]
64. Liu, Y.; Qiu, G.; Liu, Y.; Niu, Y.; Qu, R.; Ji, C.; Wang, Y.; Zhang, Y.; Sun, C. Fabrication of CoFe-MOF materials by different methods and adsorption properties for Congo red. *J. Mol. Liq.* **2022**, *360*, 119405. [CrossRef]
65. Wu, J.; Wang, J.; Du, Y.; Li, H.; Jia, X. Adsorption mechanism and kinetics of azo dye chemicals on oxide nanotubes: A case study using porous CeO_2 nanotubes. *J. Nanopart. Res.* **2016**, *18*, 191. [CrossRef]
66. Bai, Z.; Zheng, Y.; Zhang, Z. One-pot synthesis of highly efficient MgO for the removal of Congo red in aqueous solution. *J. Mater. Chem. A* **2017**, *5*, 6630–6637. [CrossRef]
67. He, Z.; Wu, F.; Guan, S.; Liu, L.; Li, J.; Huang, Y. Polyamide amine/aramid nanofiber composite aerogels as an ultra-high capacity adsorbent for Congo red removal. *J. Mater. Chem. A* **2021**, *9*, 13320–13331. [CrossRef]
68. Feng, Y.; Wang, H.; Xu, J.; Du, X.; Cheng, X.; Du, Z.; Wang, H. Fabrication of MXene/PEI functionalized sodium alginate aerogel and its excellent adsorption behavior for Cr(VI) and Congo Red from aqueous solution. *J. Hazard. Mater.* **2021**, *416*, 125777. [CrossRef]

69. Zhang, P.; Ma, X.; Guo, Y.; Cheng, Q.; Yang, L. Size-controlled synthesis of hierarchical NiO hollow microspheres and the adsorption for Congo red in water. *Chem. Eng. J.* **2012**, *189–190*, 188–195. [CrossRef]
70. Zhang, X.; Tran, H.N.; Liu, Y.; Yang, C.; Zhang, T.; Guo, J.; Zhu, W.; Ahmad, M.; Xiao, H.; Song, J. Nitrogen-doped magnetic biochar made with $K_3[Fe(C_2O_4)_3]$ to adsorb dyes: Experimental approach and density functional theory modeling. *J. Clean. Prod.* **2023**, *383*, 135527. [CrossRef]
71. Wang, C.; Liu, K.; Wang, D.; Wang, G.; Chu, P.K.; Meng, Z.; Wang, X. Hierarchical CuO–ZnO/SiO_2 Fibrous Membranes for Efficient Removal of Congo Red and 4-Nitrophenol from Water. *Adv. Fiber Mater.* **2022**, *4*, 1069–1080. [CrossRef]
72. Hou, Z.; Lan, H.; Zhu, K.; An, X.; Liu, H.; Qu, J. Hierarchically porous carbon derived from pore remodeling of waste polymeric membranes for high-efficiency adsorption applications. *Resour. Conserv. Recycl.* **2023**, *190*, 106845. [CrossRef]

Disclaimer/Publisher's Note: The statements, opinions and data contained in all publications are solely those of the individual author(s) and contributor(s) and not of MDPI and/or the editor(s). MDPI and/or the editor(s) disclaim responsibility for any injury to people or property resulting from any ideas, methods, instructions or products referred to in the content.